Lumen Segmentation in Intravascular Optical Coherence Tomography Using Backscattering Tracked and Initialized Random Walks

Abhijit Guha Roy, *Student Member, IEEE*, Sailesh Conjeti, *Student Member, IEEE*, Stéphane G. Carlier, Pranab K. Dutta, *Member, IEEE*, Adnan Kastrati, Andrew F. Laine, *Fellow, IEEE*, Nassir Navab, Amin Katouzian, and Debdoot Sheet, *Member, IEEE*

***Abstract*—Intravascular imaging using ultrasound or optical coherence tomography (OCT) is predominantly used to adjunct clinical information in interventional cardiology. OCT provides high-resolution images for detailed investigation of atherosclerosis-induced thickening of the lumen wall resulting in arterial blockage and triggering acute coronary events. However, the stochastic uncertainty of speckles limits effective visual investigation over large volume of pullback data, and clinicians are challenged by their inability to investigate subtle variations in the lumen topology associated with plaque vulnerability and onset of necrosis. This paper presents a lumen segmentation method using OCT imaging physics-based graph representation of signals and random walks image segmentation approaches. The edge weights in the graph are assigned incorporating OCT signal attenuation physics models. Optical backscattering maxima is tracked along each A-scan of OCT and is subsequently refined using global graylevel statistics and used for initializing seeds for the random walks image segmentation. Accuracy of lumen versus *tunica* segmentation has been measured on 15 *in vitro* and 6 *in vivo* pullbacks, each with 150–200 frames using 1) Cohen's kappa coefficient (0.9786 ± 0.0061) measured with respect to cardiologist's annotation and 2) divergence of histogram of the segments computed with Kullback–Leibler (5.17 ± 2.39) and Bhattacharya measures (0.56 ± 0.28). High segmentation accuracy and consistency substantiates the characteristics of this method to reliably segment lumen across pullbacks in the presence of vulnerability cues and necrotic pool and has a deterministic finite time-complexity. This paper in general also illustrates the development of methods and framework for tissue classification and segmentation incorporating cues of tissue–energy interaction physics in imaging.**

***Index Terms*—Intravascular imaging, lumen segmentation, optical backscattering physics, optical coherence tomography, random walks.**

Manuscript received November 20, 2014; revised February 5, 2015; accepted February 9, 2015. Date of publication February 12, 2015; date of current version March 3, 2016.

A. Guha Roy, P. K. Dutta, and D. Sheet are with the Department of Electrical Engineering, Indian Institute of Technology Kharagpur, Kharagpur 721302, India (e-mail: abhi4ssj@gmail.com; pkd@ee.iitkgp.ernet.in; debdoot@ee.iitkgp.ernet.in).

S. Conjeti, A. Kastrati, N. Navab, and A. Katouzian are with Technische Universität München, 80333 Munich, Germany (e-mail: sailcon.131@gmail.com; kastrati@dhm.mhn.de; nassir.navab@tum.de; amin.katouzian@cs.tum.edu).

S. G. Carlier is with the Department of Cardiology, Hôpital Ambroise Paré and Université de Mons, B-7000 Mons, Belgium (e-mail: sgcarlier@hotmail.com).

A. F. Laine is with Columbia University, New York, NY 10027 USA (e-mail: laine@columbia.edu).

Color versions of one or more of the figures in this paper are available online at http://ieeexplore.ieee.org.

Digital Object Identifier 10.1109/JBHI.2015.2403713

I. Introduction

Cardiovascular diseases increasingly account for most deaths globally and is estimated to annually account for 23.3 million by 2030 [1]. Atherosclerosis is a medical condition caused by thickening of the arterial wall (*tunica media* or *t. media*) due to excessive deposition of extracellular contents like lipids and calcium forming plaques between the *tunica intima* and *tunica media*. This thickening of *tunica intima* subsequently leads to decrease of the lumen area and eventually leads to partial or complete blockage of blood flowing through the artery [2]. Presence of untreated plaques over prolonged periods leads to onset of necrosis in lipid rich regions that often triggers vulnerability. It can lead to unstable or stable *angina pectoris* (chest pain or discomfort), *myocardial infarction* (heart attack), and sudden death due to full occlusion of a coronary artery when a vascular plaque ruptures [3]. Coronary angiography is generally the corner stone for primary diagnosis and localization of plaques within the artery. Due to their limited spatial resolution and inability to visualize the plaque, adjunct imaging with intravascular optical coherence tomography (OCT) [4]–[6] or intravascular imaging using ultrasound (IVUS) [2] is additionally performed for high-resolution imaging and detailed investigation.

OCT uses the principle of speckle formation through coherence sensing in photons backscattered by a highly scattering optical media, viz. biological tissues [7]. Intravascular imaging is carried out using a catheter mounted system which is used for high-resolution (10–20 μm) cross-sectional imaging of the artery up to depth of 0.5–2.0 mm. These characteristics make it more preferable compared to IVUS since it allows clinicians to assess symptomatic cues of plaque vulnerability like the thin-cap fibroatheroma rupture [4]. However, the spatiotemporal nonstationarity and stochastic uncertainty of speckle appearance in OCT causes visual discomfort to the clinical interpreter and limits effective use of the method for high-throughput deployment across multiple centers. This has motivated substantial research in developing computer-based methods of image segmentation [8], [9], classification and tissue characterization [4]–[6], [10], [11] for assisting clinicians with high-throughput screening. A predominant challenge still remains while imaging and analyzing thin-cap fibroatheromatous plaques where the necrotic pool is present very close to the lumen and the stochastic of associated speckles are very different. Most tissue characterization algorithms [4]–[6], [10] require cues about the lumen boundary for effective functioning and a clinician manually annotates region of interest on the images for computer-based investigation, while currently available methods for automatic lumen segmentation in OCT images [8], [9] are limited in their ability to 1) reliably segment lumen in presence of thin-cap fibroatheroma; 2) require manual initialization; and 3) iterative and do not have deterministic time complexity.

This paper presents an algorithm for reliable segmentation of lumen in sequence of OCT images of atherosclerotic arteries in the presence of vulnerability cues like thin-cap fibroatheromatous plaques. The problem of lumen segmentation is formally defined in Section II. The algorithm detailed in Section III is modeled using a random walks graph-based representation of the OCT data incorporating photon propagation physics and optical backscattering in biological tissues. Section IV presents experimental results along with evaluation of lumen segmentation accuracy. The results and different characteristics of the algorithm are discussed in Section V. Finally, we conclude the work elucidating its translating potential in Section VI. Implementation of this framework is also made available.[1]

II. Formal Definition

Let us consider an intravascular OCT image $\mathcal{I}$ such that intensity at a location $\mathbf{x}$ be $i(\mathbf{x})$. The objective of lumen segmentation is to split $\mathcal{I}$ into two disjoint sets $\mathcal{I}_{\text{lumen}}$ and $\mathcal{I}_{tunica}$ such that $\mathcal{I}_{\text{lumen}} \cap \mathcal{I}_{tunica} = \emptyset$ and $\mathcal{I}_{tunica} = \mathcal{I} - \mathcal{I}_{\text{lumen}}$. We define $\mathcal{I}$ as an equivalent graph G such that the nodes of G represent each $\mathbf{x} \in \mathcal{I}$ and the edges connecting the nodes of G are modeled, incorporating physics of photon propagation and attenuation within highly scattering biological tissues. The probability of each node of G is obtained by solving it using the random walks for image segmentation approach [12]. The class posterior probability of a location $\mathbf{x}$ is the probability of the corresponding node in G and the pixel at $\mathbf{x}$ is labeled as $\arg\max\{p(\text{lumen}|\mathbf{x},\mathcal{I}), p(tunica|\mathbf{x},\mathcal{I})\}$.

Further, in order to achieve solution to the random walks, a set of seeds $\mathcal{M}$ constituting some of the marked nodes of G such that $\mathcal{M} \subseteq \{(\mathcal{M} \in \mathcal{I}_{\text{lumen}}) \cup (\mathcal{M} \in \mathcal{I}_{tunica})\}$ and $(\mathcal{M} \in \mathcal{I}_{\text{lumen}}) \cap (\mathcal{M} \in \mathcal{I}_{tunica}) = \emptyset$ is defined for initialization using physics-based models of photon backscattering in biological tissues that influence OCT speckle formation and imaging. The random walks solver would assign class posterior probability to the unmarked nodes $\mathcal{U} = \mathcal{I} - \mathcal{M}$ to achieve the lumen segmentation task such that $\mathcal{I} \subseteq \{\mathcal{M} \cup \mathcal{U}\}$ and $\mathcal{M} \cap \mathcal{U} = \emptyset$. Fig. 1 illustrates the different stages of our proposed algorithm that are detailed in the subsequent sections.

III. Exposition to the Solution

OCT relies on the basic principle of using low time-coherence interferometry depth scans performed in the time domain for image formation [13]. A Michelson's interferometer is illuminated by a broadband low time-coherence light source which splits the incident light into the sample and reference beams with fields E_S and E_R, respectively. E_S focuses through the scanning optics and objective lens to the tissue constituting the artery being images. A modified field U_S is returned by backscattering from the tissues, while the reference field reflected from the depth scan mirror is U_R. The field from reference arm corresponds to a large phasor $U_R = A_R \exp[j(\alpha - \Omega t)]$, where A_R is the field amplitude, Ω is the phase change introduced by pulsation of the depth scan mirror, and α is the complex phase residual in the source beam. The field from the sample beam is made up of a small random phasor $U_S = A_T \exp(j\beta)$, where A_T is the field amplitude and β is the phase associated with the backscattering media viz. tissues being images. The photodetector is sensitive to the resultant intensity $I_T = U_T U_T^*$, where the detected time coherence field is $U_T = U_R + U_S = A_T \exp(j\theta)$ and U_T^* is the complex conjugate of U_T. The most relevant for OCT imaging is the phase difference ϕ between U_R and U_S such that the phasor summation of the intensity sensed at the detector can be written as

$$I_T = (U_R + U_S)(U_R + U_S)^* = A_R^2 + A_S^2 - 2A_R A_S \cos\phi \tag{1}$$

where $\phi = \beta - \alpha - \Omega t$ and the effective OCT signal is obtained after bandpass filtering to remove the constant intensity terms. Since the coherence length of the imaging setup exceeds a few wavelengths, the phase difference $\beta - \alpha \simeq \beta$ remains constant during a few rotations of U_S. The rotation of U_S at a frequency of $\frac{\Omega}{2\pi}$ permits the phasors' alignment during each measurement since U_S takes a positive and real value in each cycle at $\phi = 0$. Thus, the demodulated signal amplitude is given as $S_{\text{OCT}} = 2A_R A_S$ [13], [14].

Let I_S be the set of speckle intensity acquired by OCT at a point; then, it is known to be negative exponentially distributed [15]

$$p(I_S) = \frac{1}{\sigma_S} \exp\left(-\frac{I_S}{\sigma_S}\right) \tag{2}$$

where σ_S is the variance of I_S [15]. Since intravascular OCT is acquired using a rotatory scanning mechanism, the acquired data are stored in polar domain and a location is specified using $\mathbf{s} = (s_a, s_\theta)$, where s_a represents the distance of a scanning location from the start of the A-scanline and s_θ represents the angular displacement of the A-scanline w.r.t the starting scanline in the rotatory scan. Further, each location $\mathbf{x}$ in the Cartesian coordinate space is associated with the polar space as $\mathbf{x} = T_{\text{pol2cart}}(\mathbf{s})$ and also an inverse relation $T_{\text{cart2pol}}(\cdot) = T^{-1}_{\text{pol2cart}}(\cdot)$ exists. Since the speckle intensity $I_S(\cdot)$ has a high dynamic range, it is generally compressed nonlinearly to a lower dynamic range signal $i(\cdot)$ to form the B-mode image, and they are related as

$$i(\cdot) = p_1 + p_2 \log_{10}(I_S(\cdot) + p_3) \tag{3}$$

where p_1, p_2 and p_3 are empirically determined constants [16] and $i(\mathbf{x}) \in \mathcal{I}$ [see Fig. 1(c)] represents the OCT image in Cartesian coordinate space as defined earlier. Equivalently, $I_S(\mathbf{x})$ [see Fig. 1(a)] and $I_S(\mathbf{s})$ [see Fig. 1(b)], respectively, represent the

[1] http://www.facweb.iitkgp.ernet.in/~debdoot/downloads/OCTLumSegRW.zip

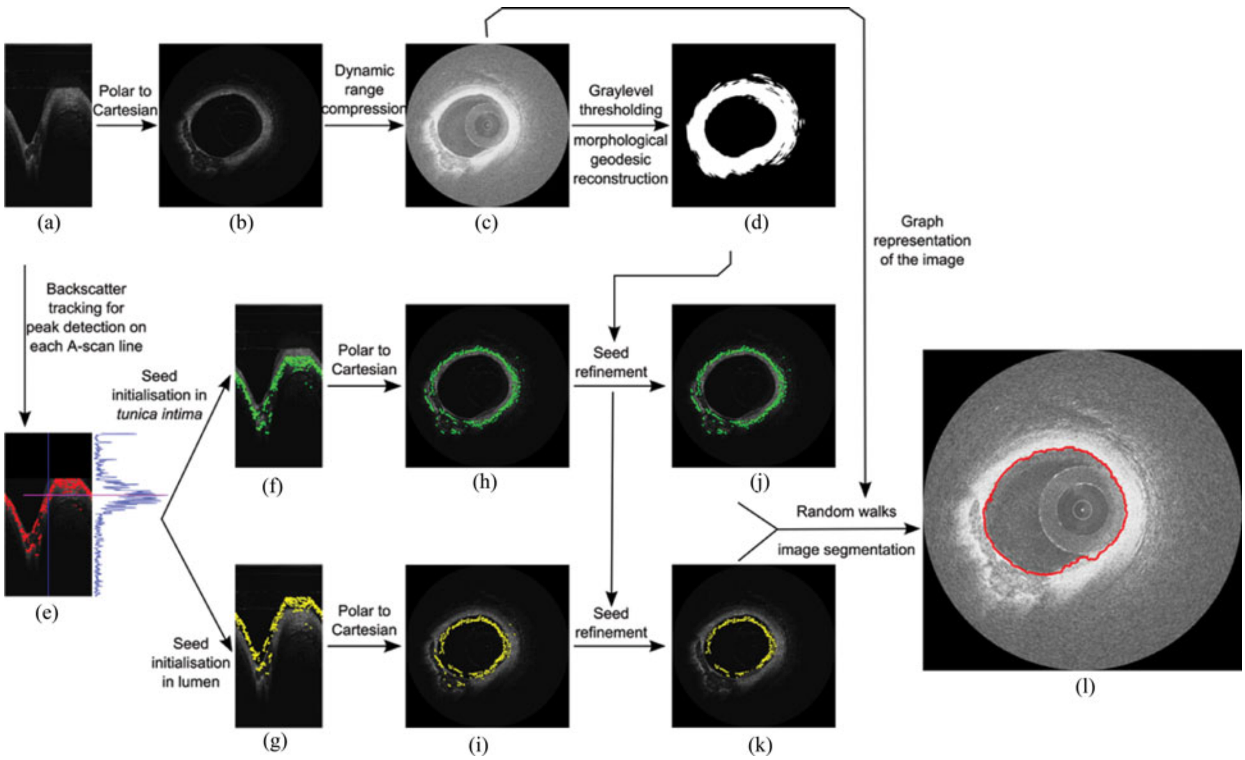

Fig. 1. Illustration of the different stages involved in our approach for lumen segmentation in intravascular OCT image. (a) IV-OCT speckle data (16bpp), (b) IV-OCT speckle data (16bpp), (c) Log compressed (B-mode) IV-OCT data, (d) Approximate mask of tunica intima, (e) Maxima tracked along each A-scan line for seed localization, (f) Initial estimate of seeds in tunica intima, (g) Initial estimate of seeds in lumen, (h) Initial estimate of seeds in tunica intima, (i) Initial estimate of seeds in lumen, (j) Refined estimate of seeds in tunica, (k) Refined estimate of seeds in lumen, (l) Detected lumen boundary.

uncompressed speckle intensity in Cartesian coordinate space and in polar space.

A. Graph Representation of the Image

Let an OCT image $\mathcal{I}$ be represented as an undirected graph G, where it is defined as $G = (V, E)$ with vertices $v \in V$ and edge $e \in E \in V \times V$. The edge e connecting two vertices v_p and v_q is denoted as e_{pq} and is assigned a weight $w_{pq} > 0$. The degree of the vertex at p is given by $d_p = \sum w_{pq}$ for all edges e_{pq} connected with v_p. Considering 4-adjacency of the pixels in $\mathcal{I}$ such that $(p, q) \in V$ are adjacent pixels in $\mathcal{I}$, the edge weights are defined following the physics of photon intensity attenuation in OCT imaging [13]

$$w_{pq} = \begin{cases} \exp\left(-\eta|z_p - z_q|\right), & \text{if } p \text{ and } q \text{ are adjacent} \\ 0, & \text{otherwise} \end{cases} \tag{4}$$

where η is an empirically defined constant and its value depends on the models of photon intensity attenuation in OCT imaging. z_p and z_q are intensities of the pixels corresponding to vertices (p, q) in $\mathcal{I}$ and are illustrated in Fig. 2.

B. Seed Initialization in Lumen and Tunica

The intensity of OCT signal $I_S(\mathbf{s})$ at any point along the scanline is highest when $\phi \to 0$ in (1). In the demodulated signal amplitude S_{OCT}, this condition indicates the highest value of the field amplitudes A_S and arises when at $\mathbf{s}$ there is a sharp change of refractive index of the media through which the photons are traveling. In intravascular OCT, the sharp changes occur at the boundary of lumen and *tunica intima*, a thin layer of epithelial cells laminating the vascular cavity and the muscular *tunica media* [4]. At all other points following the maxima along the A-scanline s_θ, the intensity of the OCT speckle signal decays exponentially until a further sharp change of refractive index in the media [5], [11], [17].

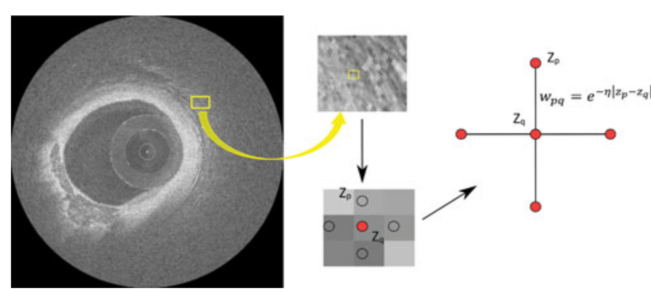

Fig. 2. Equivalent graph representation of the OCT image $\mathcal{I}$.

This model of optical backscattering is used for finding the initial estimate of boundary seeds [see Fig. 1(e)] on the region between lumen and *tunica intima*

$$\mathbf{s}_{\text{boundary}} = \left\{ \arg\max_{s_a} \left(I_S(\mathbf{s})\right) \right\} \quad \forall s_\theta \in I_S. \tag{5}$$

However, in the presence of stochastic uncertainty associated with nonstationary speckles in OCT as mentioned in (2), the initial estimate of seeds is not always error free as illustrated in Fig. 3. This estimate is subsequently used to obtain an initial

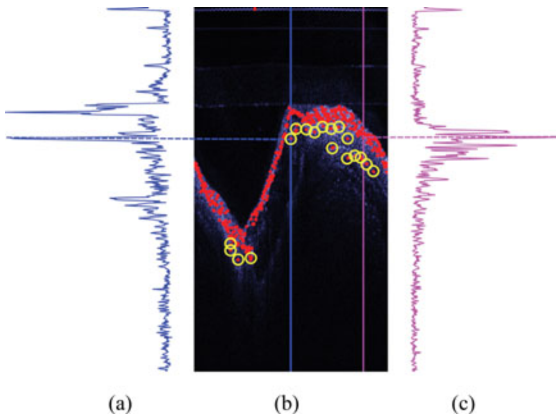

Fig. 3. Error in initial location of *tunica intima* seeds selected by tracking of maxima along each A-scanline. (a) A-scanline with maxima tracked at location other than on lumen boundary. (b) Maxima points detected along each A-scanline and erroneous points encircled. (c) A-scanline with maxima tracked at correct location on lumen boundary.

estimate of seeds in *tunica* [see Fig. 1(f) and (h)] and lumen [see Fig. 1(g) and (i)]

$$\mathbf{s}_{\text{lumen}} = \{(s_a - a_1, s_\theta)\} \quad \forall (s_a, s_\theta) \in \mathbf{s}_{\text{boundary}} \tag{6}$$

$$\mathbf{s}_{tunica} = \{(s_a + a_2, s_\theta)\} \quad \forall (s_a, s_\theta) \in \mathbf{s}_{\text{boundary}} \tag{7}$$

where a_1 and a_2 are two empirically chosen constants and the initial estimates are used to obtain the set of marked nodes $\mathcal{M}$ after refinement as present in the subsequent section.

C. Refinement of Lumen and Tunica Seeds

The *tunica* is formed of endothelial cells, muscle fibers, and muscle tissue, epithelial cells in healthy arteries, and extracellular plaque constituents during atherosclerosis. The densely placed fibrous tissues in the pool of extracellular matrix causes intermittent change of refractive index leading to $\phi \to 0$ and high value of the field amplitude A_S in (1) thus giving rise to high speckle intensity I_S and $i(\mathbf{x}) \in \mathcal{I}$ [13], [14]. This generally forms a bimodal distribution of the probability density of $\mathcal{I}$ that is used for determining the speckle rich region $\mathcal{B}_S$ constituting *tunica* in major and the complementary region $\mathcal{B}_{\bar{S}}$ constituting the lumen as deeper regions within *tunica* where heavy signal attenuation limits speckle formation such that $\mathcal{B}_S \cap \mathcal{B}_{\bar{S}} = \emptyset$ and $\mathcal{B}_S \cup \mathcal{B}_{\bar{S}} = \mathcal{I}$:

$$\mathcal{B}_S = \arg_{\mathbf{x} \in \mathcal{I}} \{\mathcal{I} \geq \tau\} \tag{8}$$

where τ is obtained following the method in [18] and an example of $\mathcal{B}_S$ post-morphological geodesic reconstruction is illustrated in Fig. 1(d). The marked nodes $\mathcal{M}$ [see Fig. 1(j) and (k)] for initializing random walks solver on G are hence obtained as

$$\mathcal{M} \in \mathcal{I}_{\text{lumen}} = \mathbf{s}_{\text{lumen}} \cap \mathcal{B}_{\bar{S}} \tag{9}$$

$$\mathcal{M} \in \mathcal{I}_{\text{tunica}} = \mathbf{s}_{\text{tunica}} \cap \mathcal{B}_S. \tag{10}$$

D. Solution to Random Walks for Lumen Segmentation

The graph G is represented as a combinatorial Laplacian matrix L for achieving an analytically convergent solution [12]

$$L_{pq} = \begin{cases} d_p, & \text{if } p = q \\ -w_{pq}, & \text{if } v_p \text{ and } v_q \text{ are adjacent nodes} \\ 0, & \text{otherwise} \end{cases} \tag{11}$$

where L_{pq} is indexed by vertices v_p and v_q. The set of vertices or nodes V can be divided into two groups:

(1) $V_M \in \mathcal{M}$ consisting of marked or seeded nodes;
(2) $V_U \in \mathcal{U}$ consisting of unmarked or unseeded nodes;

such that $V_M \cup V_U = V$ and $V_M \cap V_U = \emptyset$. Thus, the Laplacian matrix can be decomposed as

$$L = \begin{bmatrix} L_M & B \\ B^T & L_U \end{bmatrix} \tag{12}$$

where L_M and L_U are Laplacian submatrices corresponding to V_M and V_U, respectively. We denote the probability of a random walker starting at a node v_q to reach a seeded point belonging to tissue type $\omega \in \{\text{lumen}, tunica\}$ as x_q^ω s.t. $\sum_\omega x_q^\omega = 1$. Further, to achieve a solution, the set of labels defined for all the seeds in $V_M \in \mathcal{M}$ is specified using a function

$$Q(v_q) = \omega \quad \forall v_q \in V_M \tag{13}$$

where $\omega \in \mathbb{Z}$, $0 < \omega \leq 2$ s.t. $\omega = 1$ is the set of label corresponding to $\mathcal{I}_{\text{lumen}}$, and $\omega = 2$ is the set of labels corresponding to $\mathcal{I}_{tunica}$. This helps us in defining $M \in \mathcal{M}$ is a 1-D vector of $|V_M| \times 1$ elements corresponding to each label s at node $v_q \in V_M$ constituted as

$$m_q^\omega = \begin{cases} 1, & \text{if } Q(v_q) = \omega \\ 0, & \text{if } Q(v_q) \neq \omega. \end{cases} \tag{14}$$

Therefore, for label ω, the solution can be obtained by solving

$$L_U x_q^\omega = -B^T m_q^\omega \tag{15}$$

$$L_U X = -B^T M \tag{16}$$

where solving for $\omega = 1$ yields $X = \{x_q \forall q | v_q \in V\}$ as the set of solution probabilities of a random walker originating at a node $q \in G$ and reaching the lumen and is associated and solved accordingly

$$p(\text{lumen}|\mathbf{x}, \mathcal{I}) = x_q^\omega \forall \{q \in G \Leftrightarrow \mathbf{x} \in \mathcal{I}\}, \omega = 1 \tag{17}$$

$$p(tunica|\mathbf{x}, \mathcal{I}) = 1 - p(\text{lumen}|\mathbf{x}, \mathcal{I}) \tag{18}$$

$$\mathcal{I}_{\text{lumen}} = \left\{ \arg\max_{\omega, \mathbf{x}} (p(\omega|\mathbf{x}, \mathcal{I})) = \text{lumen} \right\}. \tag{19}$$

IV. Experiments and Results

A. OCT Data Collection

1) In vitro: Human coronary arterial segments were obtained from anonymous autopsy examinations, less than 12 h past death at the New York Presbyterian Hospital/Columbia

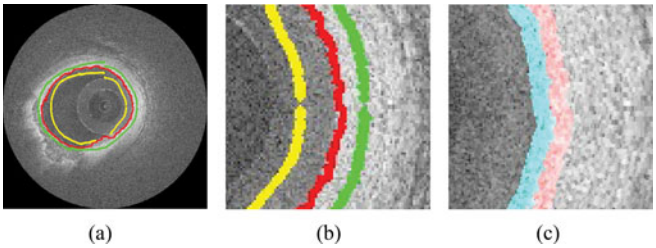

Fig. 4. Illustration of the different regions around the detected lumen boundary used for quantifying the accuracy between the two regions. (a) Detected lumen boundary (red) with the seeds for lumen (yellow) and *tunica* (green). (b) Magnified view of the lumen boundary (red) and the seeds for lumen (yellow) and *tunica* (green). (c) Thin neighborhood around the detected lumen boundary within lumen $\mathcal{N}_{\mathrm{lumen}}$ (cyan) and within *tunica* $\mathcal{N}_{tunica}$ (red).

University Medical School, NY, USA. To prevent artery contraction and deformation, the hearts were pressure-fixed before excision using 10% formalin, recirculating at 100 mmHg for 2 h. Artery segments presenting significant plaque accumulation were identified and excised. During *in vitro* OCT imaging, the artery segments were immersed in a bath of 0.9% NaCl solution maintained at $37\,^{\circ}$C. The arteries were imaged with a rotary catheter based Fourier-domain OCT system[2] with a center wavelength of 1320 nm and axial resolution of 7.3μm in air (5.4μm in tissue) and segments with symptomatic thin-cap fibroatheroma were also identified. Details of data acquisition and histological correlation are available in [4].

2) In vivo: OCT imaging on six follow-up patients with stents implanted in coronary arteries was performed with a Fourier-domain OCT system with same specifications as used for *in vitro* data. The details of data acquisition are available in [6].

B. Implementation

Data acquired *in vitro* from 15 artery segments and *in vivo* from six arteries symptomatic of atherosclerotic plaque formation and thin-cap fibrotheroma were used for our experiments. Each pullback of OCT data consisted of 150–300 frames. Each frame of OCT signal I_S acquired in polar domain consisted of 400 A-scanlines s.t. $|s_\theta| = 400$ and had 752 samples along each A-scanline s.t. $|s_a| = 752$. The polar domain data are converted to Cartesian coordinate space of size 512×512. The values for the nonlinear compression in (3) are $p_1 = 0$, $p_2 = 1$, and $p_3 = 10$. The constant $\eta = 90$ in (4). The empirically chosen constants $a_1 = 10$ in (6) and $a_2 = 20$ in (7). The random walks solution is obtained using [12].[3]

C. Quantification of Segmentation Accuracy

1) Divergence of Speckle Intensity Between Segments: Unsupervised evaluation is done by comparing the statistical divergence [19] between the distribution of intensity values of $\mathcal{I}$ in a thin neighborhood around the lumen boundary in the segmented result, with $\mathcal{N}_{\mathrm{lumen}}$ located within the lumen and having pdf Q and $\mathcal{N}_{tunica}$ located within the *tunica* and having pdf P. Fig. 4 illustrates the selection of the different regions used, and the following measures used for divergence computation are reported for the complete dataset in Table I.

TABLE I
STATISTICAL DIVERGENCE BETWEEN PDF OF INTENSITY VALUES IN $\mathcal{N}_{\mathrm{lumen}}$ AND $\mathcal{N}_{\mathrm{tunica}}$ INDICATING ACCURACY OF LUMEN DETECTION IN INTRAVASCULAR OCT DATA

Divergence measure	Our approach	[17]
Kullback–Leibler distance	5.1735 ± 2.39	4.2211 ± 6.99
Bhattacharya distance	0.5641 ± 0.2822	0.2653 ± 0.3649

TABLE II
SUPERVISED EVALUATION OF SEGMENTATION ACCURACY

Measure	Our approach	[17]
Cohen's Kappa coefficient	0.9786 ± 0.0061	0.8692 ± 0.0709
Contour RMS Error	8.4655 ± 3.8540	52.0845 ± 20.4840

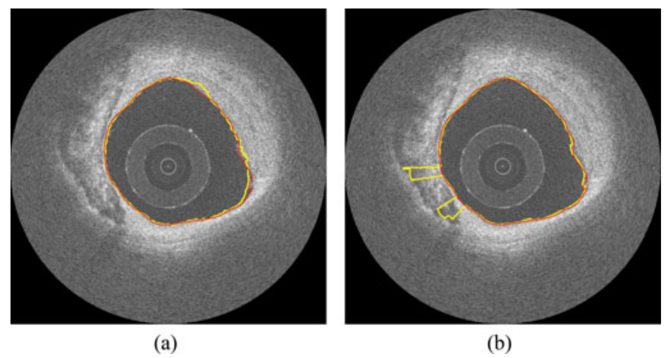

Fig. 5. Comparison of results obtained with our approach and prior art [17]. The expert annotated ground truth (red) and segmentation result (yellow) are marked. The failure of prior art to segment in presence of necrotic pool is evident. (a) Our approach ($\kappa = 0.9797$). (b) Prior art [17] ($\kappa = 0.9621$).

(1) Kullback–Leibler divergence

$$d_{KL} = \sum_{i=1}^{g} P(i) \ln \left(\frac{P(i)}{Q(i)} \right) \tag{20}$$

(2) Bhattacharya distance

$$d_B = -\ln \left[\sum_{i=1}^{g} \left(\sqrt{P(i) Q(i)} \right) \right] \tag{21}$$

where g is the total number of graylevels considered while computing the pdf and $g = 256$ in our experiments where $\mathcal{I}$ is an 8 bpp image.

2) Kappa Coefficient for Comparison of Interannotator Variability: Supervised evaluation of the segmentation results in contrast with ground truths annotated by an experienced Cardiologist is performed using the Cohen's Kappa coefficient (κ) [20]. The ground truth lumen boundaries were annotated on 41 different OCT frames. Further, the contour RMS error between the manually annotated lumen contour and segmentation results (Fig. 5.) was also computed and performance of our approach in comparison with [17] is presented in Table II.

[2]C7-XR, LightLab Imaging Inc., Westford, MA, USA.
[3]http://cns.bu.edu/ lgrady/software.html

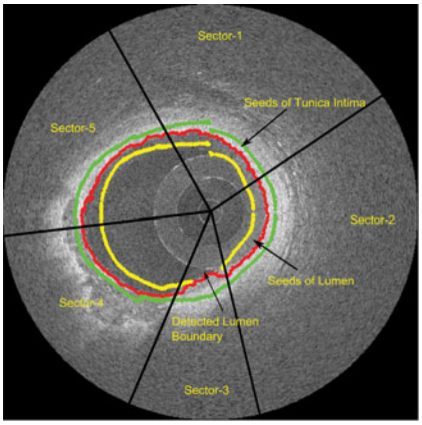

Fig. 6. Result of lumen detection in a sample with sparse seeds. The image is divided in to five sectors and the seeds of lumen (yellow) and *tunica intima* (green) are marked.

TABLE III
STATISTICAL DIVERGENCE BETWEEN PDF OF INTENSITY VALUES IN $\mathcal{N}_{\mathrm{lumen}}$ AND $\mathcal{N}_{\mathrm{tunica}}$ IN THE FIVE SECTORS MARKED IN FIG. 6

Divergence measure	Sec. 1	Sec. 2	Sec. 3	Sec. 4	Sec. 5
Kullback–Leibler distance	4.12	2.44	0.94	3.97	2.91
Bhattacharya distance	3.05	0.1027	2.1715	2.3714	0.08

V. DISCUSSION

A. Boundary Detection in Presence of Sparse Seeds

One of the characteristics of this algorithm is its ability to refine the placement of seeds in lumen and *tunica* (see Section III-C) for obtaining an accurate random walks solution of the detected lumen boundary. In certain situations, this leads to discontinuity of seeds place in the lumen, and despite this, the algorithm is expected to perform accurately. Fig. 6 elucidates some of such scenarios and the reliability of this algorithm to accurately detect lumen boundary despite such limitations. Sector 1 has an evident discontinuity in the contour of seeds in lumen and *tunica*. Sector 2 has minor discontinuity in the seeds of lumen. Sector 3 has a complete stretch of nonexistent seeds of lumen. Sectors 4 and 5 present complete continuity of seeds, while Sector 4 is also characterized by presence of calcification. The detected lumen boundary contours in all the five sectors are visually evident to accurately follow the actual lumen boundary. Further, there is no observed discontinuity between the detected contour in these regions. Table III presents the divergence measures of segmentation accuracy in all the five sectors in Fig. 6 to substantiate their consistency and reliability.

B. Interframe Consistency of Lumen Detection

An important characteristic desired in any lumen detection algorithm is consistency of detection across adjacent frames to ensure smooth transverse section profile of the imaged vessel. This property is evaluated following the framework in Fig. 7. We have considered an intravascular OCT stack of 200 frames for one pullback data. A transverse section is sliced out from

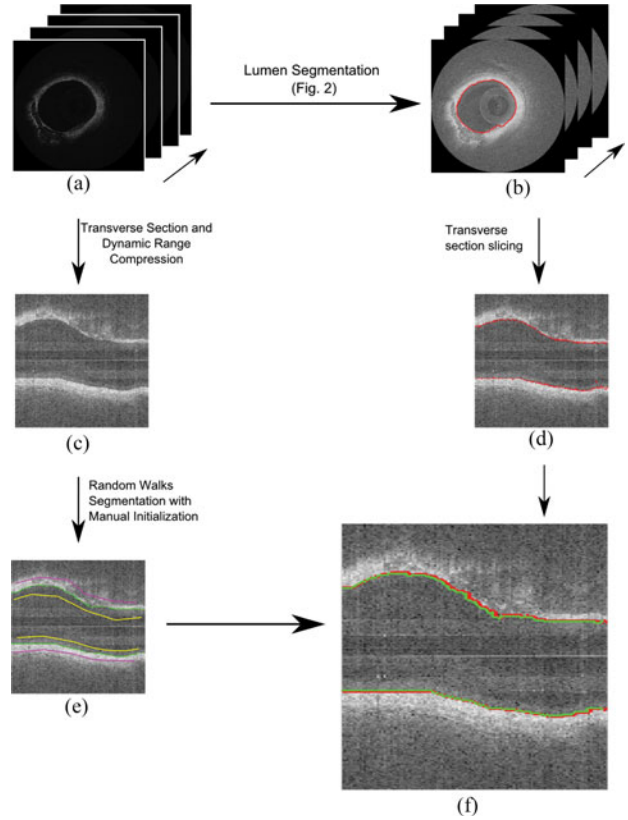

Fig. 7. Result of interframe consistency of lumen boundary detection. (a) Stack of IV-OCT frames (16bpp), (b) Detected Lumen Boundary, (c) Transverse Section of IV-OCT frames (8bpp), (d) Detected Lumen Boundary in Transverse Section, (e) Segmented Lumen Boundary (green) with manually initialized seeds for Lumen (yellow) and tunica intima (magenta), (f) Comparison of Consistency of detected Lumen boundary (red) accross frames in contract with manual segmentation (green).

this stack [see Fig. 7(c)] and the lumen boundary is detected in it using manually seeded random walks [see Fig. 7(e)]. This resultant contour is compared with the contour observed by transverse sectioning of the lumen contour map in the detected results [see Fig. 7(d)]. The comparison is presented in Fig. 7(f). The mean squared error between these two lumen contours is computed to be limited with displacement of 2.01 pixels and evidently substantiates the claim of interframe consistency of detected lumen boundary.

C. Reliable Detection in Plaques of Different Sizes and Shapes

Another important characteristic desired in any lumen boundary detection algorithm is its ability to perform with equal reliability across multiple shapes and sizes of plaques images with intravascular OCT. Fig. 8 illustrates this ability of this algorithm. The segmentation accuracy in these two OCT images is presented in Table IV and their consistency strongly substantiates this ability of the algorithm.

D. Effect of Guide-Wire and Stent Strut Shadows

A major challenge in lumen segmentation is the presence of shadows due to the guide-wire and stent struts during *in vivo*

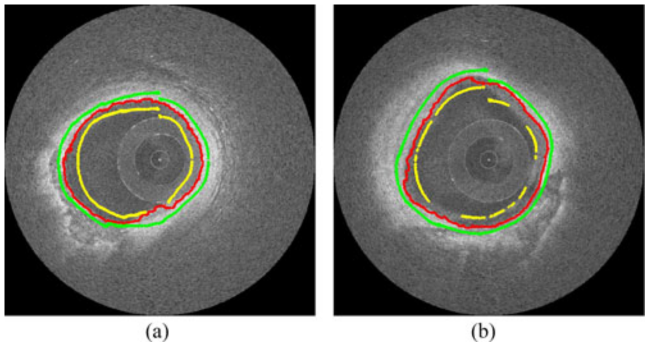

Fig. 8. Illustration of reliable lumen boundary detection across plaques of different shapes and sizes. (a) Section with small lumen size. (b) Section with larger lumen size.

TABLE IV
STATISTICAL DIVERGENCE BETWEEN PDF OF INTENSITY VALUES IN $\mathcal{N}_{\rm lumen}$ AND $\mathcal{N}_{\rm tunica}$ IN FIG. 8

Divergence measure	Fig. 8(a)	Fig. 8(b)
Kullback–Leibler distance	12.1649	7.6227
Bhattacharya distance	0.6841	0.3785

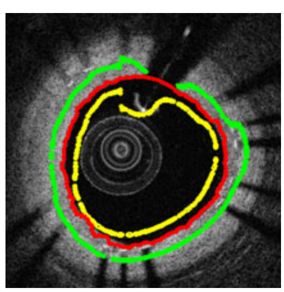

Fig. 9. Reliable lumen boundary detection in *in vivo* OCT images in presence of guide-wire and stent strut shadows. The seeds of lumen (yellow), *tunica* (green) and segmented lumen boundary (red) are marked.

imaging. Fig. 9 illustrates the characteristics of our approach to accurately segment the lumen in the presence of such artifacts.

E. Computational Time

The proposed algorithm was implemented in MATLAB r2013b and executed on a laptop computer with Intel Core i3 @ 2.50-GHz CPU, 4.00 GB of RAM, and Windows 8 (64 bits) operating system. Per frame processing time was 18.82 ± 1.77 s when tested over 30 frames of OCT pullback data.

VI. CONCLUSION

This paper presents a computationally efficient and reliable algorithm for completely automated and user-interaction free lumen boundary detection in intravascular OCT image sequences. The algorithm models the problem as a graph-based segmentation approach and uses cues of tissue–photon interaction in OCT for creating the model, thus contributing in its high accuracy and reliability. Initially, the OCT data acquired in polar domain are converted to Cartesian coordinate space and its speckle intensity is nonlinearly compressed to a lower dynamic range. This is subsequently modeled as a 2-D graph with four-neighbor adjacency between the nodes and the edge weights are modeled following speckle intensity attenuation physics of OCT signals. The solution to segmentation is obtained using a random walks solver, where the initial estimates of seeds for lumen and *tunica* are provided by estimating them from backscattering properties along each A-scanline and through refinement in the presence of stochastic uncertainty of OCT speckle intensity. The segmented lumen boundary in OCT data of 15 *in vitro* and six *in vivo* pullbacks each with 150–300 frames has been assessed to be highly accurate as indicated by quantified scores of statistical divergence measures and interannotator variability comparison with Cohen's Kappa coefficient. The method also demonstrates 1) reliable lumen segmentation in the presence of different tissues under the lumen border, 2) interframe consistency of detected lumen, 3) ability to segment lumen over wide shape and size variations, 4) reliability in presence of guide-wire and stent strut shadows, and 5) deterministic and finite time complexity and assured convergent results [12]. These characteristics make it unique and provide it with an edge compared to other state-of-the-art methods of lumen segmentation. Furthermore, this framework also presents rational incorporation of OCT imaging physics into each stage of the algorithm to compensate for uncertainty inherent to tissue–energy interaction physics of the imaging modality.

REFERENCES

[1] S. C. Smith, A. Collins, R. Ferrari, D. R. Holmes, S. Logstrup, D. V. McGhie, J. Ralston, R. L. Sacco, H. Stam, and K. Taubert, "Our time: A call to save preventable death from cardiovascular disease (heart disease and stroke)," *J. Am. Coll. Cardiol.*, vol. 60, no. 22, pp. 2343–2348, 2012.

[2] J. S. Suri, C. Kathuria, and F. Molinari, Eds., *Atherosclerosis Disease Management*. New York, NY, USA: Springer, 2010.

[3] J. Narula, M. Nakano, R. Virmani, F. D. Kolodgie, R. Petersen, R. Newcomb, S. Malik, V. Fuster, and A. V. Finn, "Histopathologic characteristics of atherosclerotic coronary disease and implications of the findings for the invasive and noninvasive detection of vulnerable plaques," *J. Am. Coll., Cardiol.*, vol. 61, no. 10, pp. 1041–1051, 2013.

[4] C. Xu, S. G. Carlier, R. Virmani, and J. M. Schmitt, "Characterization of atherosclerosis plaques by measuring both backscattering and attenuation coefficients in optical coherence tomography," *J. Biomed. Opt.*, vol. 13, no. 3, p. 034003, 2008.

[5] F. J. van der Meer, D. J. Faber, D. B. Sassoon, M. C. Aalders, G. Pasterkamp, and T. G. van Leeuwen, "Localized measurement of optical attenuation coefficients of atherosclerotic plaque constituents by quantitative optical coherence tomography," *IEEE Trans. Med. Imag.*, vol. 24, no. 10, pp. 1369–1376, Oct. 2005.

[6] C. Malle, T. Tada, K. Steigerwald, G. J. Ughi, T. Schuster, M. Nakano, S. Massberg, J. Jehle, G. Guagliumi, A. Kastrati, R. Virmani, R. A. Byrne, and M. Joner, "Tissue characterization after drug-eluting stent implantation using optical coherence tomography," *Arteriosclerosis, Thrombosis, Vascular Biol.*, vol. 33, no. 6, pp. 1376–1383, 2013.

[7] D. Huang, E. A. Swanson, C. P. Lin, J. S. Schuman, W. G. Stinson, W. Chang, M. R. Hee, T. Flotte, K. Gregory, C. A. Puliafito, and J. G. Fujimoto, "Optical coherence tomography," *Science*, vol. 254, no. 5035, pp. 1178–1181, 1991.

[8] M. Moraes, C. Cardoso, A. C. Diego, and S. S. Furuie, "Automatic lumen segmentation in IVOCT images using binary morphological reconstruction," *Biomed. Eng. Online*, vol. 12, p. 78, Jan. 2013.

[9] S. Tsantis, G. C. Kagadis, K. Katsanos, D. Karnabatidis, G. Bourantas, and G. C. Nikiforidis, "Automatic vessel lumen segmentation and stent strut detection in intravascular optical coherence tomography," *Med. Phys.*, vol. 39, no. 1, pp. 503–13, Jan. 2012.

[10] S. Celi and S. Berti, "In-vivo segmentation and quantification of coronary lesions by optical coherence tomography images for a lesion type definition and stenosis grading," *Med. Image Anal.*, vol. 18, no. 7, pp. 1157–1168, 2014.

[11] G. J. Ughi, K. Steigerwald, T. Adriaenssens, W. Desmet, G. Guagliumi, M. Joner, and J. Dhooge, "Automatic characterization of neointimal tissue by intravascular optical coherence tomography," *J. Biomed. Opt.*, vol. 19, no. 2, pp. 021 104–021 104, 2014.

[12] L. Grady, "Random walks for image segmentation," *IEEE Trans. Pattern Anal., Mach. Intell.*, vol. 28, no. 11, pp. 1768–1783, Nov. 2006.

[13] A. F. Fercher, W. Drexler, C. K. Hitzenberger, and T. Lasser, "Optical coherence tomography-principles and applications," *Rep., Prog., Phys.*, vol. 66, no. 2, p. 239, 2003.

[14] J. M. Schmitt, "Optical coherence tomography (OCT): A review," *IEEE J. Sel. Topics, Quantum Electron.*, vol. 5, no. 4, pp. 1205–1215, Jul./Aug. 1999.

[15] M. Bashkansky and J. Reintjes, "Statistics and reduction of speckle in optical coherence tomography," *Opt. Lett.*, vol. 25, no. 8, pp. 545–547, 2000.

[16] D. Kaplan and Q. Ma, "On the statistical characteristics of log-compressed rayleigh signals: Theoretical formulation and experimental results," in *Proc. IEEE Ultrason. Symp.*, Oct. 1993, pp. 961–964.

[17] G. J. Ughi, T. Adriaenssens, P. Sinnaeve, W. Desmet, and J. Dhooge, "Automated tissue characterization of in vivo atherosclerotic plaques by intravascular optical coherence tomography images," *Biomed. Opt. Exp.*, vol. 4, no. 7, pp. 1014–1030, 2013.

[18] N. Otsu, "A threshold selection method from gray-level histograms," *Automatica*, vol. 11, nos. 285–296, pp. 23–27, 1975.

[19] S. Cha, "Comprehensive survey on distance/similarity measures between probability density functions," *Int. J. Math. Models, Methods, Appl. Sci.*, vol. 1, no. 4, pp. 300–307, 2007.

[20] J. Cohen, "A coefficient of agreement for nominal scales," *Educ. Psychol. Meas.*, vol. 20, no. 1, pp. 37–46, Apr. 1960.

Abhijit Guha Roy (S'15) was born in Baripada, India in 1989. He received the B.E. degree in electrical engineering from Jadavpur University, Kolkata, India, in 2012. He has been working toward the M.Tech. degree in instrumentation and signal processing at the Indian Institute of Technology Kharagpur, Kharagpur, India, since 2013.

He is also a DAAD Visiting Student at the Technishe Universität München, München, Germany. His research interests include computational medical imaging, machine learning, and medical image computing.

Sailesh Conjeti (S'11) was born in Chennai, India, in 1990. He received the B.E.(Hons.) degree in electrical and electronics engineering from the Birla Institute of Technology and Science, Pilani, India, in 2012, the M.Tech. degree in medical imaging and informatics from the Indian Institute of Technology Kharagpur, Kharagpur, India, in 2014. He is currently a doctoral student at the Chair for Computer Aided Medical Procedures at Technishe Universität München, München, Germany.

His research interests include computational medical imaging, machine learning, medical image computing, and biomedical signal processing.

Stéphane G. Carlier received the M.D. degree from the Université Libre de Bruxelles, Brussel, Belgium, in 1996, and the Ph.D. degree in biomedical engineering from Erasmus University, Rotterdam, Netherlands, in 2001.

He is currently an Interventional Cardiologist at Hôpital Ambroise Paré and a Professor of cardiology at the Université de Mons (UMons), Mons, Belgium. He was an Assistant Professor of clinical medicine at Columbia University, New York, NY, USA and the Director of the Intravascular Imaging and Physiology Corelab of the Cardiovascular Research Foundation. His research interests include intravascular imaging, cardiac and vascular dynamics, physiology, and signal processing.

Dr. Carlier is a Member of the European Association of Percutaneous Cardiovascular Interventions of the European Society of Cardiology.

Pranab K. Dutta (M'10) received the B.E. degree in electrical engineering from Bengal Engineering College, Shibpur, India, in 1984, the M.E. degree in electrical engineering from the University of Calcutta, Kolkata, India, in 1986, and the Ph.D. degree in electrical engineering from the Indian Institute of Technology Kharagpur, Kharagpur, India, in 1992.

He has been a Professor at the Department of Electrical Engineering, since 2004, and the Head of the School of Medical Science and Technology, since 2009, at the Indian Institute of Technology Kharagpur, where he joined as a Lecturer in 1993. His main research interests include optical imaging, image processing, and machine learning for biomedical applications.

Adnan Kastrati studied medicine in Tirana, Albania, where he graduated in 1979. He trained as a specialist and completed his postdoctoral studies in 1988.

He was an Alexander von Humboldt Researcher at Heidelberg University, Germany, and Technishe Universität München (TUM), Germany. Prior to his appointment to the Chair of Internal Medicine at TUM, since 2000, he has worked as a Visiting Researcher at the German Cardiac Center in Munich (DHM). He is currently a Chief Physician and Deputy Director of the Cardiovascular Disease Clinic at DHM and Director of the Cardiac Catheter Laboratory and the ISARESEARCH Center. His research focus is on optimizing treatment strategies in patients with acute coronary syndrome and in developing new drug-coated stents with an improved safety and efficacy profile.

Andrew F. Laine (S'82–M'83–SM'07–F'10) received the B.S. degree from Cornell University, Ithaca, NY, USA, in 1977, and the D.Sc. degree from Washington University, St. Louis, MO, USA, in 1989.

He is currently with the Department of Biomedical Engineering, Columbia University, New York, NY, USA. He is the President of the IEEE Engineering in Medicine and Biology Society (EMBS) (2015–2016), has served as the Chair of Technical Committee on Biomedical Imaging and Image Processing for the EMBS (2006–2009), and is on the IEEE ISBI steering committee since 2006. His research interests include quantitative image analysis; cardiac functional imaging: ultrasound and MRI, retinal imaging, intravascular imaging and biosignal processing. He is a Fellow of the American Institute for Medical and Biological Engineering.

Nassir Navab received the Diploma degree in computer engineering from the University of Technology of Compiégne, Compiégne, France, in 1988, and the Ph.D. from INRIA, Paris, France, in 1993.

He is currently a Chair Professor for computer aided medical procedures and a Professor at the School of Medicine, Technical University of Munich, Germany; Professor of Computer Science at the Johns Hopkins University, Baltimore, MD, USA. His research interests include surgical workflow, registration/visualization, segmentation, reconstruction, medical imaging, molecular imaging, computer-aided surgery, patient monitoring, computer vision, industrial augmented reality, medical augmented reality, and machine learning for medical applications.

Dr. Navab is an Associate Editor for the IEEE TRANSACTIONS ON MEDICAL IMAGING, *Medical Physics*, and on the Editorial Board of *Medical Image Analysis* and *International Journal Computer Vision*. He is also a Fellow of the MICCAI Society.

Amin Katouzian received the B.S. degree from Sistan and Baluchestan University, Sistan Va Baluchestan, Iran, and the M.S. degree from Fairleigh Dickinson University, NJ, USA, in 1998 and 2004, respectively, both in electrical engineering, and the Ph.D. degree in biomedical engineering from Columbia University, New York, NY, USA in 2011. During his Ph.D., he developed algorithms for ultrasound-based tissue characterization of atherosclerotic plaques.

He has been a Senior Research Scientist at the Chair for Computer Aided Medical Procedures, Technical University of Munich, Munich, Germany, since 2011. His research interests include multidimensional medical image and signal analysis, computer-aided diagnosis and surgery, pattern recognition, and understanding of sensory data within surgical workflows.

Debdoot Sheet (S'09–M'14) was born in Kharagpur, India, in 1986. He received the B.Tech. degree in electronics and communication engineering from the West Bengal University of Technology, Kolkata, India, in 2008, the M.S. and Ph.D. degrees in medical imaging from the Indian Institute of Technology Kharagpur, Kharagpur, India, in 2010 and 2014, respectively.

He was a DAAD Visiting Scholar at the Chair for Computer Aided Medical Procedures, Technishe Universität München, München, Germany, during 2011–2012. He is currently an Assistant Professor of electrical engineering at the Indian Institute of Technology Kharagpur. His research interests include computational medical imaging, machine learning, image and multidimensional signal processing, and visualization. He has been a Regional Editor of IEEE PULSE since 2014.